Adjoint-based sensitivity analysis of a differentially-heated cavity

Technical Report 2068625-TN-09
Deliverable 5.3

Josh Williams,[*] Ubaid Ali Qadri,[†] Sue Thorne[‡]

March 4, 2024

1 Introduction

Tokamak reactors aim to use confined plasma to create energy by nuclear fusion [Nordlund et al., 2018]. Due to the complex combination of interactions at multiple length-scales, flow instabilities can arise that cause reduced performance and damage to the reactor's walls [Luce, 2011; Mordijck, 2022]. The interplay between multiple interacting design and operating parameters creates a difficult optimisation problem to maximise power output of future tokamak reactors. Additionally, the complex plasma flow is prone to instabilities that limit the confinement achieved by tokamaks. Identifying the onset of instabilities and developing passive/active control strategies is therefore crucial for the success of nuclear fusion reactors. The adjoint method has been used extensively in stability analysis, uncertainty quantification, optimisation and control problems [Magri, 2019; Kord and Capecelatro, 2019; Qadri et al., 2021]. Applications and recent developments in the adjoint method for NEPTUNE-related problems were reviewed in our report [Williams et al., 2023].

In this report, we aimed to study the stability of a differentially-heated cavity at Rayleigh numbers near the stability frontier. We study the adjoint global mode alongside the direct mode obtained from classic linear stability analysis to identify the most sensitive region of the flow (called the 'wavemaker' by Giannetti and Luchini [2007]. The sensitivity of the eigenvalue to changes in the wall temperature are evaluated with varying top and bottom boundary conditions. The proxy-app accompanying this report (deliverable 5.2) can be found at `https://github.com/ExCALIBUR-NEPTUNE/NumericalAnalysis/tree/main/Adjoint`.

2 Methods

2.1 Flow configuration

We consider a differentially-heated square cavity with a heated left wall ($T_L = 1$), a cold right wall ($T_R = 0$) and gravity acting in the vertical direction (Figure 1a). The working fluid is air ($Pr = 0.71$), under the Boussinesq approximation where the temperature acts on the velocity only through a buoyancy term (density and viscosity are constant). We use the non-dimensional equations given by Le Quéré and Behnia [1998] as

$$\nabla \cdot \boldsymbol{u} = 0 \tag{1a}$$

$$\frac{\partial \boldsymbol{u}}{\partial t} + \boldsymbol{u} \cdot \nabla \boldsymbol{u} = -\nabla p + \frac{Pr}{\sqrt{Ra}} \nabla^2 \boldsymbol{u} + PrT\boldsymbol{y} \tag{1b}$$

$$\frac{\partial T}{\partial t} + \boldsymbol{u} \cdot \nabla T = \frac{1}{\sqrt{Ra}} \nabla^2 T. \tag{1c}$$

---

[*]Josh Williams is with the Hartree Centre, STFC Royal Observatory Edinburgh, Blackford Hill, Edinburgh, EH9 3HJ, UK.

[†]Ubaid Ali Qadri is with the Hartree Centre, STFC Daresbury Laboratory, Warrington, UK.

[‡]Sue Thorne is with the Hartree Centre, STFC Rutherford Appleton Laboratory, Harwell, UK.
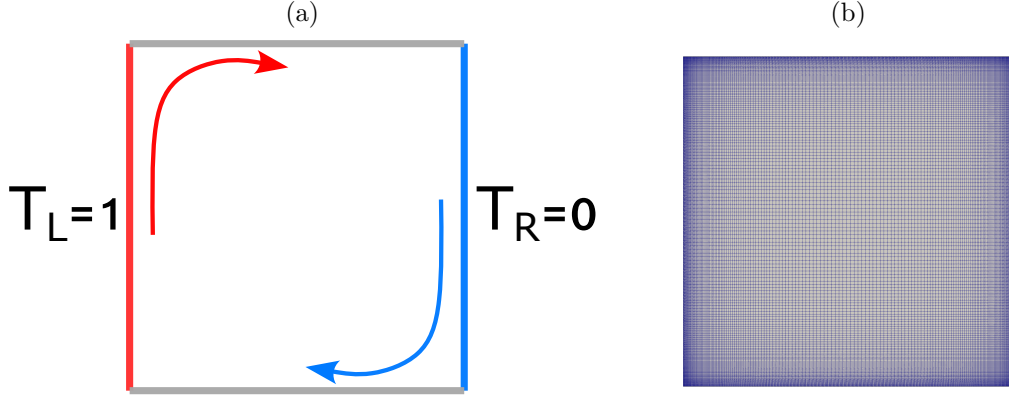
Figure 1: Flow configuration (a) and wall-refined mesh (b) for differentially heated cavity problem. Arrows in panel (a) indicate the direction of fluid motion due to the buoyancy force (gravity acting downwards). Grey lines on the top and bottom boundaries are used as these can be assigned to be conducting or insulating. Left and right boundaries always use Dirichlet boundary conditions with $T_L = 1$ and $T_R = 0$.
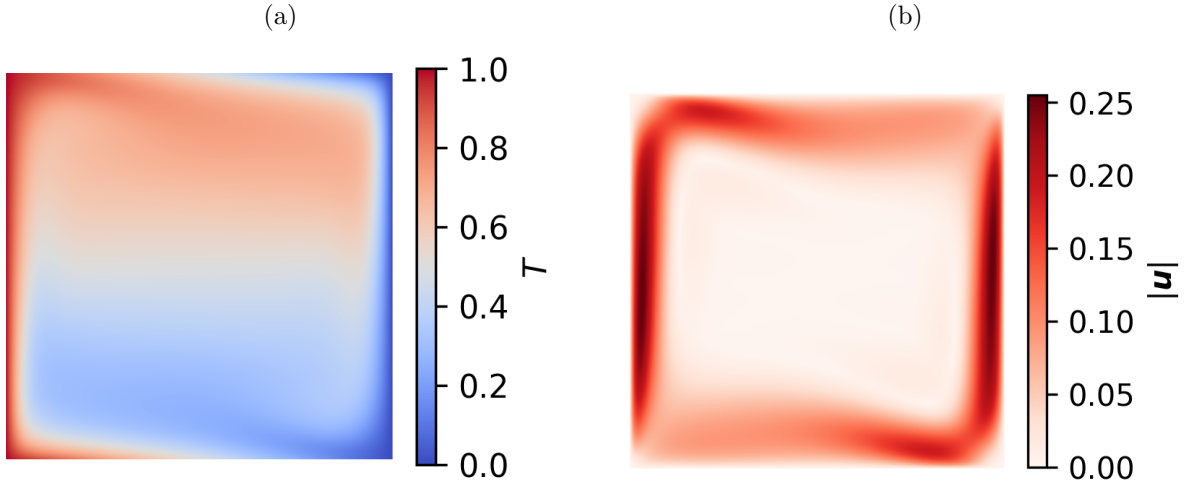

Figure 2: Baseflow from vertical slot convection with conducting top and bottom boundary conditions at $Ra = 2.1 \times 10^6$ and $Pr = 0.71$. Panels show (a) temperature and (b) velocity.

All simulations were performed in Nektar++ (https://www.nektar.info) [Cantwell et al., 2015; Moxey et al., 2020] using a wall-refined mesh (Figure 1b) and a polynomial order 6.

For the top and bottom boundaries, we considered conducting and insulating boundary conditions for temperature. From results reported by UKAEA [Threlfall et al., 2023], the conducting boundary conditions yields a lower critical Rayleigh number, Ra_c and a simpler stability frontier. The conducting boundary conditions give a linear variation of T across the top and bottom boundaries [Saglietti et al., 2017]

$$T_T(x) = T_B = T_L - \Delta T(x/L), \qquad (2)$$

where T_T and T_B are the temperatures on the top and bottom boundaries, respectively. ΔT is the temperature difference across the cavity ($\Delta T = 1$ in this study), x is the coordinate in the horizontal direction, L is the horizontal length of the cavity ($L = 1$ in this study). The critical Rayleigh number of the flow with conducting boundary conditions is $Ra_c \approx 2.1 \times 10^6$, which gave the baseflow shown in Figure 2.

The insulating boundary conditions are Neumann boundary conditions, given as

$$\boldsymbol{n} \cdot \nabla T = 0 \qquad (3)$$

at the top and bottom boundaries, where $\boldsymbol{n}$ is a unit normal vector at the boundary. The critical Rayleigh number of the flow with insulating boundary conditions is $Ra_c \approx 1.8 \times 10^8$, which gave the baseflow shown in Figure 3.
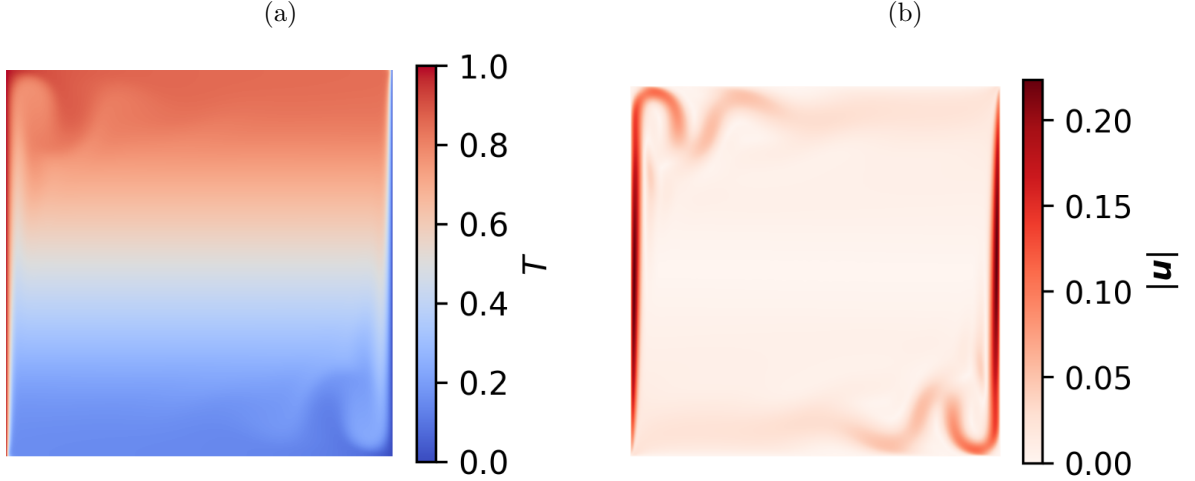
Figure 3: Baseflow from vertical slot convection with insulating top and bottom boundary conditions at $Ra = 1.8 \times 10^8$ and $Pr = 0.71$. Panels show (a) temperature and (b) velocity.

2.2 Stability analysis

The linearised equations are then

$$\nabla \cdot \boldsymbol{u}' = 0, \tag{4a}$$

$$\partial_t \boldsymbol{u}' + \overline{\boldsymbol{u}} \cdot \nabla \boldsymbol{u}' + \boldsymbol{u}' \cdot \nabla \overline{\boldsymbol{u}} = -\nabla p + \frac{Pr}{\sqrt{Ra}} \nabla^2 \boldsymbol{u}' + PrT' \boldsymbol{y}, \tag{4b}$$

$$\partial_t T' + \overline{\boldsymbol{u}} \cdot \nabla T' + \boldsymbol{u}' \cdot \nabla \overline{T} = \frac{1}{\sqrt{Ra}} \nabla^2 T', \tag{4c}$$

which can also be expressed in compact notation as

$$\partial_t \boldsymbol{q}' = \boldsymbol{L} \boldsymbol{q}' \tag{5}$$

where $\boldsymbol{q}'$ is the perturbed state vector ($\boldsymbol{q}' = [\boldsymbol{u}', T']$), and $\boldsymbol{L}$ is the linear differential operator. Eigenmodes of $\boldsymbol{q}'$ of the form $\boldsymbol{q}' = \exp(\lambda t)\hat{\boldsymbol{q}}$ are desired to assess the asymptotic stability of perturbations to the flow, where $\lambda = \sigma + i\omega$ is the complex eigenvalue and $\hat{\boldsymbol{q}} = [\hat{\boldsymbol{u}}, \hat{T}]$ is the direct global mode. The growth rate is found by $\sigma = \mathrm{Re}(\lambda)$ and frequency is $\omega = \mathrm{Im}(\lambda)$.

Similarly, we define the adjoint state-vector as $\boldsymbol{q}^+$ and the adjoint global modes as $\hat{\boldsymbol{q}}^+$. The adjoint global modes describe the *receptivity* of the system to open-loop forcing (see reviews such as Schmid and Brandt [2014], Luchini and Bottaro [2014] or Magri [2019]). From the derivation in Appendix A, the adjoint equations are

$$\nabla \cdot \boldsymbol{u}^+ = 0 \tag{6a}$$

$$\partial_t \boldsymbol{u}^+ + \overline{\boldsymbol{u}} \cdot \nabla \boldsymbol{u}^+ + \boldsymbol{u}^+ \cdot \nabla \overline{\boldsymbol{u}} = -\nabla p + \frac{Pr}{\sqrt{Ra}} \nabla^2 \boldsymbol{u}' - T^+ \nabla \overline{T} \tag{6b}$$

$$\partial_t T^+ + \overline{\boldsymbol{u}} \cdot \nabla T^+ = \frac{1}{\sqrt{Ra}} \nabla^2 T^+ + Pr \left(\boldsymbol{u}^+ \cdot \boldsymbol{y} \right) \tag{6c}$$

We are interested in perturbations to the left wall temperature, δT_L, which may act at the level of the linearised equations ($\delta T_L'$) or as a steady forcing on the baseflow ($\delta \overline{T}_L$). The former is derived in Appendix A, where the sensitivity gradient of the eigenvalue with respect to changes in T_L' is found to be

$$\partial_{T_L'} \lambda = T_L^+ = \frac{1}{\sqrt{Ra}} \nabla T^+ \cdot \boldsymbol{n} \tag{7}$$

and λ is the eigenvalue of the flow. The right-hand side can be computed from the adjoint global mode [Qadri, 2014].

The process of finding the sensitivity to steady forcing on the baseflow requires the definition of an adjoint baseflow, $\overline{\boldsymbol{q}}^+$, which is derived in subsection A.1. The adjoint baseflow equations are

$$\nabla \cdot \overline{\boldsymbol{u}}^+ = 0, \tag{8a}$$

$$\overline{\boldsymbol{u}}^+ \cdot \nabla \overline{\boldsymbol{u}} + \overline{\boldsymbol{u}} \cdot \nabla \overline{\boldsymbol{u}}^+ = -\hat{\boldsymbol{u}} \cdot \nabla \hat{\boldsymbol{u}}^+ - \hat{\boldsymbol{u}}^+ \cdot \nabla \hat{\boldsymbol{u}} - \hat{T}^+ \nabla \hat{T} - \overline{T}^+ \nabla \overline{T} + \frac{Pr}{\sqrt{Ra}} \nabla^2 \overline{\boldsymbol{u}}^+ - \nabla \overline{p}^+, \tag{8b}$$

$$\overline{\boldsymbol{u}} \cdot \nabla \overline{T}^+ = -\hat{\boldsymbol{u}} \cdot \nabla \hat{T}^+ + \frac{1}{\sqrt{Ra}} \nabla^2 \overline{T}^+ + Pr(\boldsymbol{y} \cdot \overline{\boldsymbol{u}}^+), \tag{8c}$$

where the global modes appear on the right-hand side of the momentum and temperature transport equations as forcing terms: the implementation of this in Nektar++ is described in Appendix B. Due to this, we must normalise the global modes. Following Giannetti and Luchini [2007], we normalise the direct and adjoint global modes as

$$\max_{x,y \in \Omega} |\hat{\boldsymbol{q}}(x,y)| = 1 \tag{9}$$

and

$$\langle \hat{\boldsymbol{q}}^+, \hat{\boldsymbol{q}} \rangle = 1. \tag{10}$$

The normalisations in (9) and (10) are a pre-processing step on the global modes in the process of setting up the adjoint baseflow problem. Additionally, this should be done when computing the 'wavemaker' to allow the structural sensitivity to be computed as the product of the direct and adjoint eigenmodes, $\boldsymbol{S} = \hat{\boldsymbol{q}} \hat{\boldsymbol{q}}^+$.

The adjoint baseflow wall temperature is equal to the sensitivity of the eigenvalue to perturbations in $\overline{T}_L$, which is found to be

$$\partial_{\delta \overline{T}_L} \lambda = \overline{T}_L^+ = \frac{1}{\sqrt{Ra}} \nabla \overline{T}^+. \tag{11}$$

2.3 Numerical method and verification

Eigenvalues of the direct and adjoint governing equations were found using a modified Arnoldi algorithm developed by Barkley et al. [2008] for time-stepper codes such as Nektar++. We found this to require fewer iterations of the outer loop (e.g. full computations of $\boldsymbol{q}'$ for a specified $T_{Arnoldi}$) than the commonly used ARPACK library [Lehoucq et al., 1998], making it computationally less expensive. The number of steps used to evolve the direct and adjoint equations was determined by $T_{Arnoldi}$, which we estimated to be 20% of the instability period given by Le Quéré and Behnia [1998] of 21 time units for $Ra = 1.8 \times 10^8$ with insulating boundaries. The direct and adjoint analyses used the same time-step as the forward simulations ($\Delta t = 2 \times 10^{-3}$ time units).

The accuracy of the global mode calculations can be assessed by comparing the direct and adjoint eigenvalue spectra [Saglietti et al., 2017], where the real and imaginary values of each mode should overlap. We verify this for $Pr = 0.71$ and $Ra = 1.5 \times 10^6$ with conducting boundary conditions. The rationale behind this choice is discussed below. As shown in Figure 4, the eigenvalues from the adjoint and direct analysis are in close agreement. The mean error was found to be 2.3×10^{-6}.

This accuracy of the adjoint sensitivity gradient (7) can be assessed against a gradient obtained from a finite-difference approximation [Vishnampet et al., 2015], Figure 5. The gradient error should scale linearly with the perturbed value $\delta T_L'$ or $\delta \overline{T}_L$. The change in growth rate due to deviations in the baseflow temperature, $\delta \overline{T}_L$, are then found by

$$\varepsilon = \frac{\sigma(\overline{T}_L + \delta \overline{T}_L) - \left(\sigma(\overline{T}_L) + \delta \overline{T}_L \sum \overline{T}_L^+(\boldsymbol{x}_L) \right)}{\sigma(\overline{T}_L)}. \tag{12}$$

This requires simulations of a new baseflow for each $\overline{T}_L + \delta \overline{T}_L$ value. Therefore, to minimise the computational overhead, we use the case with $Ra_c = 1.5 \times 10^6$, $Pr = 0.71$ and conducting top and bottom walls since the kinetic energy was found to decay to a constant value after a long enough time. This was advantageous as it avoided using the (adaptive) selective frequency damping method [Åkervik et al., 2006; Jordi et al., 2015], which is required to obtain a baseflow for unsteady flows and can be time-consuming to converge (although this method is used later for higher Ra baseflows).
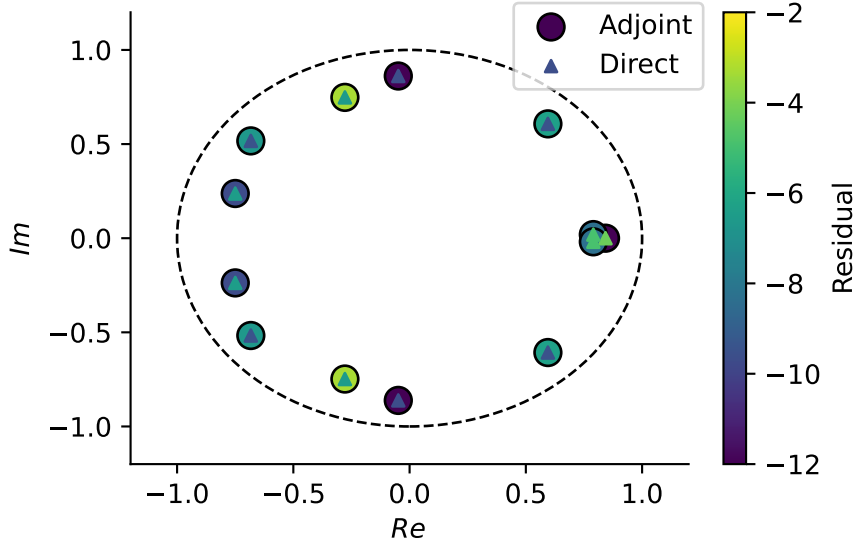
Figure 4: Real and imaginary components from adjoint and direct global modes, shown compared to a unit circle (dotted line). Tests were performed with $Ra_c = 1.5 \times 10^6$ and $Pr = 0.71$ using conducting top and bottom walls.
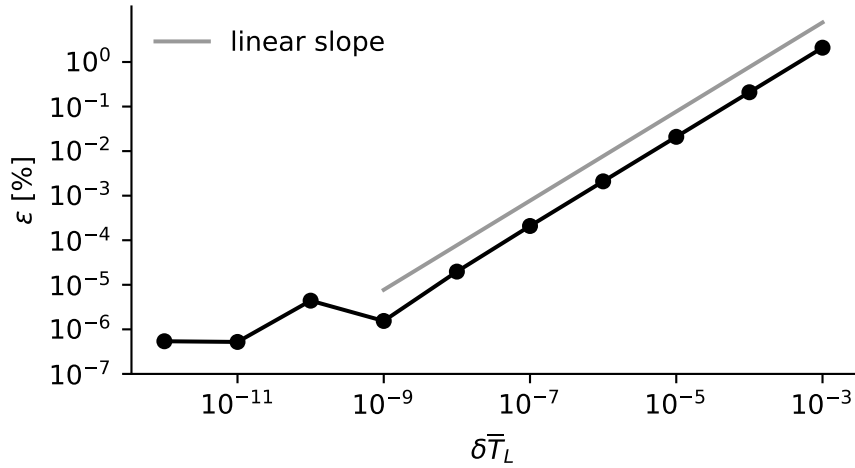

Figure 5: Error in predicted growth rate with changes in $\delta \overline{T}_L$, compared to predictions from the adjoint gradient. Tests were performed with $Ra_c = 1.5 \times 10^6$ and $Pr = 0.71$ using conducting top and bottom walls. The (logarithm) slope of errors in the range $\delta T'_L = 10^{-9} - 10^{-3}$ is linear (slope = 0.99) and becomes constant at sufficiently small perturbations as reported by Vishnampet et al. [2015].
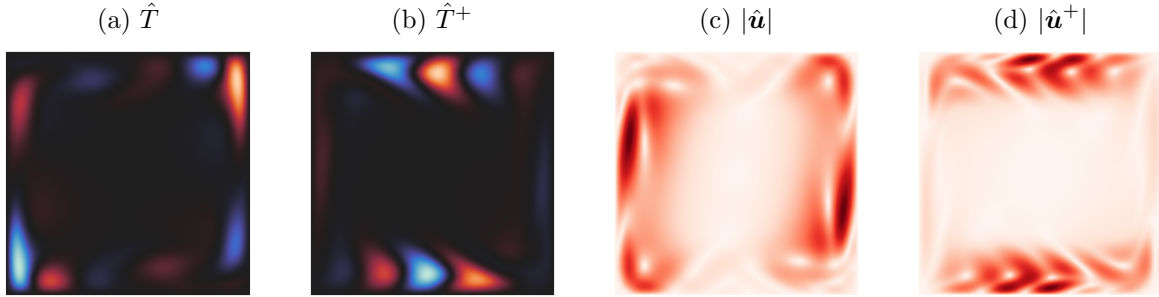
Figure 6: Adjoint and direct global modes with conducting top and bottom wall boundary conditions, near the critical Rayleigh number $Ra = 2.1 \times 10^6$, $Pr = 0.71$, replicating conditions from Saglietti et al. [2017]. Growth rate and frequency were $\sigma = 1.56 \times 10^{-3}$ and $\omega = \pm 0.229$, respectively.

3 Results

3.1 Adjoint and direct global modes

Figure 6(a,c) shows the largest magnitude direct global mode of the conducting boundary problem, which is a complex mode of $\sigma = 1.56 \times 10^{-3}$ and $\omega = \pm 0.229$. Its adjoint counterpart is shown in Figure 6(b,d). The structure of both the adjoint and direct modes are in agreement with Saglietti et al. [2017]. The direct temperature eigenmode is strongest at the start of the thermal boundary layer, whereas the direct velocity eigenmode is more intense as the boundary layer is more developed. The adjoint eigenmodes are concentrated on the horizontal walls, where the upper boundary of the baseflow shows an interface between hot fluid carried towards the cold wall by its inertia, and the cooled portion of the conducting boundary (Figure 2, upper boundary). The same is true for the lower wall, where there is an interface between the heated portion of the conducting wall and the cold fluid. The adjoint eigenmodes show that these areas are most receptive to temperature and velocity forcing.

The structural sensitivity of the conducting boundary configuration shows a weak sensitivity along the vertical boundaries (Figure 7), except for the $\hat{T} \cdot \hat{v}^+$ component, which appears to have a stabilizing effect on the eigenmode (due to the negative sign). The low sensitivity of $\hat{v}$ and $\hat{v}^+$ modes can be attributed to the adjoint modes being primarily concentrated along the horizontal boundaries. The most sensitive regions are where the boundary layer attached to the horizontal walls approaches the fixed temperature walls. This demonstrates that the detachment of the thermal boundary layer in the baseflow as the hot fluid convects towards the cooled half of the domain ($x > 0.5$) is the main source of instability.

The largest magnitude direct modes for the insulating boundary problem are shown in Figure 8 (a,c), and their adjoint in Figure 8 (b,d). Our predicted period of oscillation $\tau = 2\pi/\omega = 21.92$ agrees well with Le Quéré and Behnia [1998], who predicted τ between 21 and 22, depending on Ra. This shows the least stable region to be in the top left and lower right corners where the boundary layer detaches (Figure 3). The adjoint velocity eigenmode shows an intense thin layer on the top and bottom walls, situated near the corners, where the baseflow boundary layer separates (Figure 8d).

The structural sensitivity tensor for insulating boundary conditions demonstrates a strong sensitivity in the two opposing corners where the boundary layer detaches (Figure 9). The $\hat{u}$ and $\hat{u}^+$ modes appear to have a relatively low influence due to the coupling between T and v, and also the fact that the insulating conditions impose no thermal boundary layer on the horizontal boundaries (unlike the conducting wall configuration, Figure 7).

3.2 Sensitivity to heated wall temperature

The sensitivity of the leading eigenvalue to steady and unsteady wall temperature variations is shown in Figure 10. The conducting wall configuration shows an overall stabilizing effect on the flow for steady forcing at the bottom of the boundary (Figure 10a). Unsteady forcing provided an overall destabilizing effect on the flow, however the integral of the gradient over the wall gave a value of 0.18 and a maximum value of 0.3 which was significantly lower than the steady forcing integral of -0.8 and a (absolute) value of 4.2 (in the negative direction). This shows the largest change in eigenvalue would be obtained by steady forcing on the lower half of the wall, particularly near the onset of the boundary layer at $y \approx 0.1$. Low sensitivity to unsteady forcing was also found by Qadri [2014] when studying the effect of a heated ring in a low-density jet (Figure 4.5 in Qadri [2014]).

Figure 7: Wavemaker from vertical slot convection with conducting top and bottom boundary conditions at $Ra = 2.1 \times 10^6$ and $Pr = 0.71$.

(a) $\hat{T}$ (b) $\hat{T}^+$ (c) $|\hat{\boldsymbol{u}}|$ (d) $|\hat{\boldsymbol{u}}^+|$

Figure 8: Adjoint and direct global modes near the critical Rayleigh number $Ra = 1.8 \times 10^8$, $Pr = 0.71$, replicating conditions from Le Quéré and Behnia [1998] and Threlfall et al. [2023]. The growth rate and frequency are $\sigma = -3.5 \times 10^{-4}$, and $\omega \pm 0.29$.
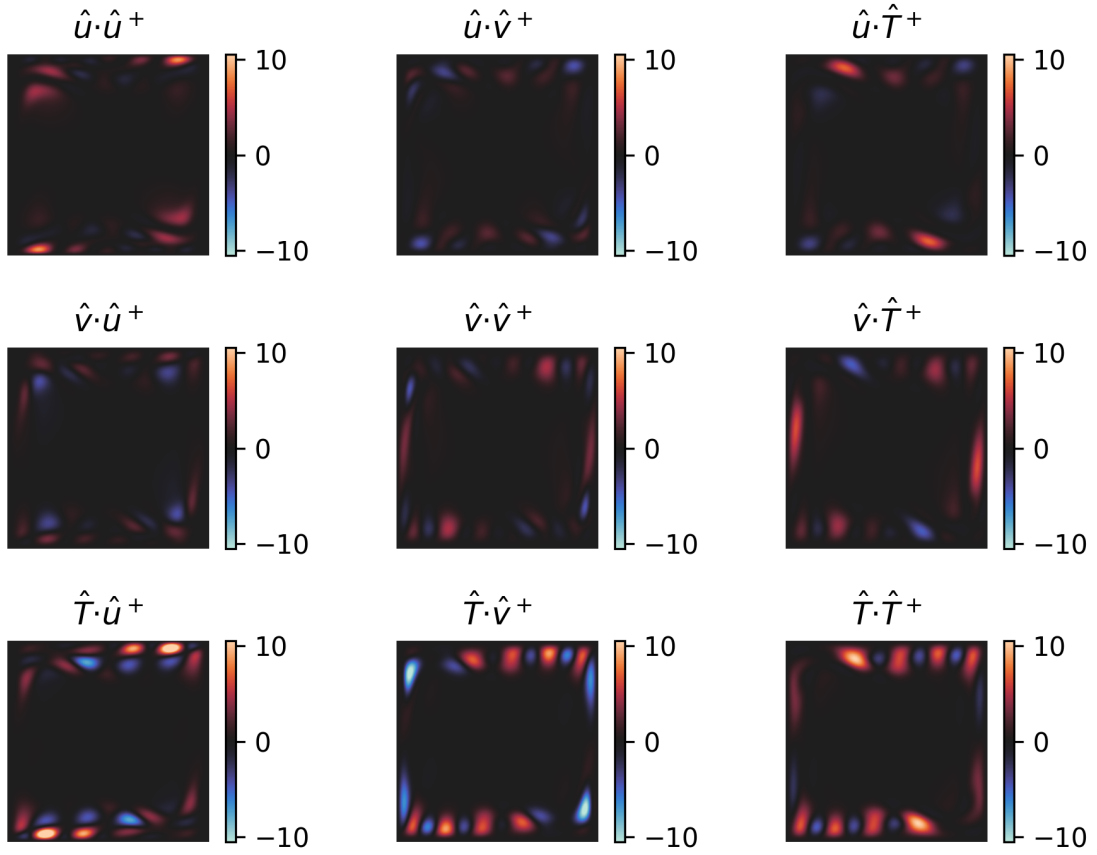
Figure 9: Wavemaker from vertical slot convection with insulating top and bottom boundary conditions at $Ra = 1.8 \times 10^8$ and $Pr = 0.71$.
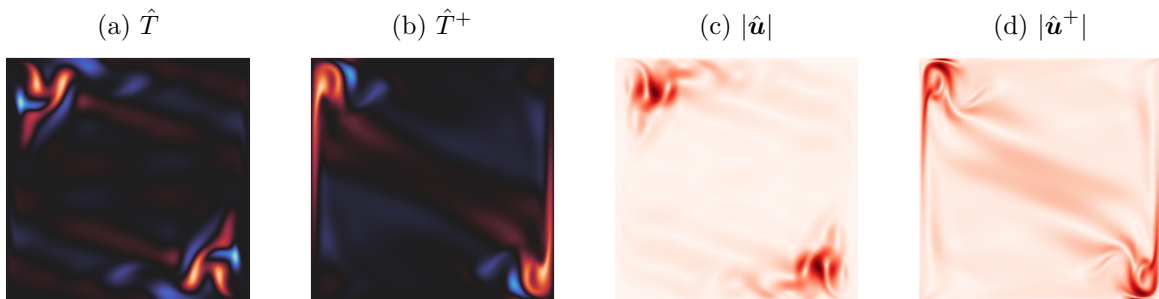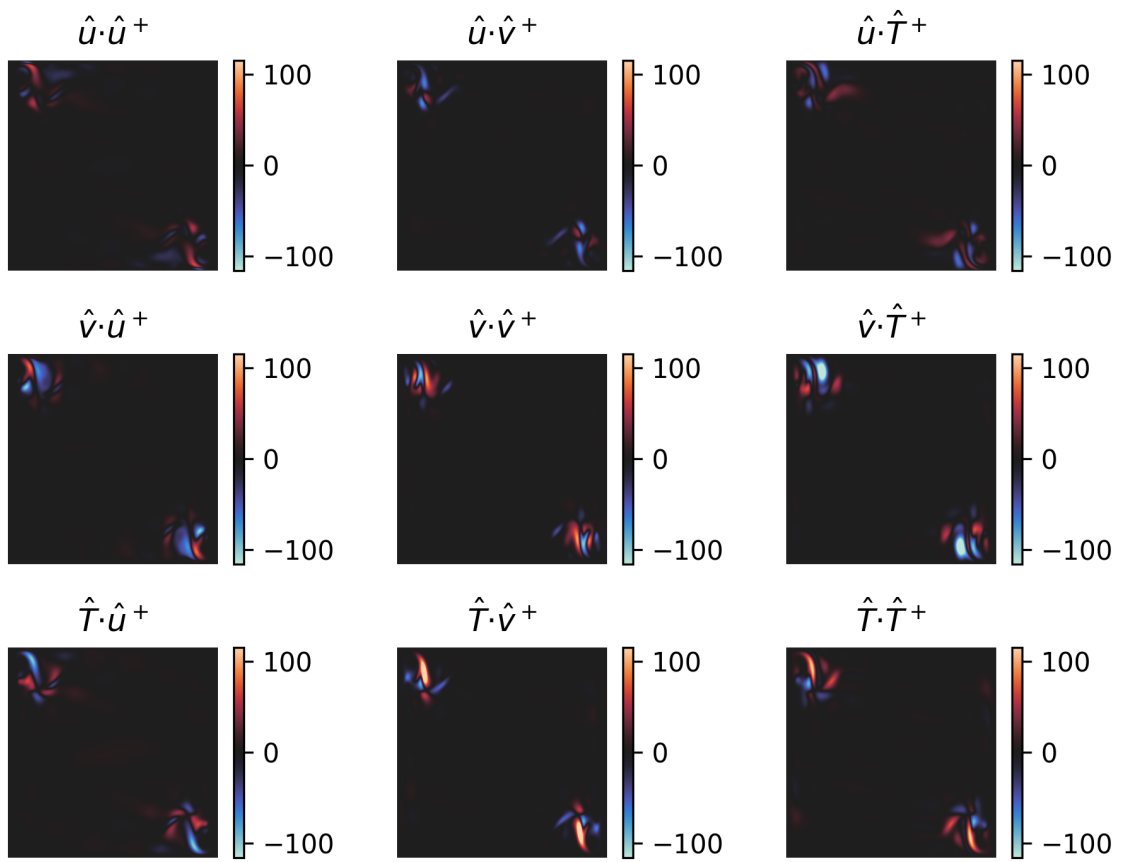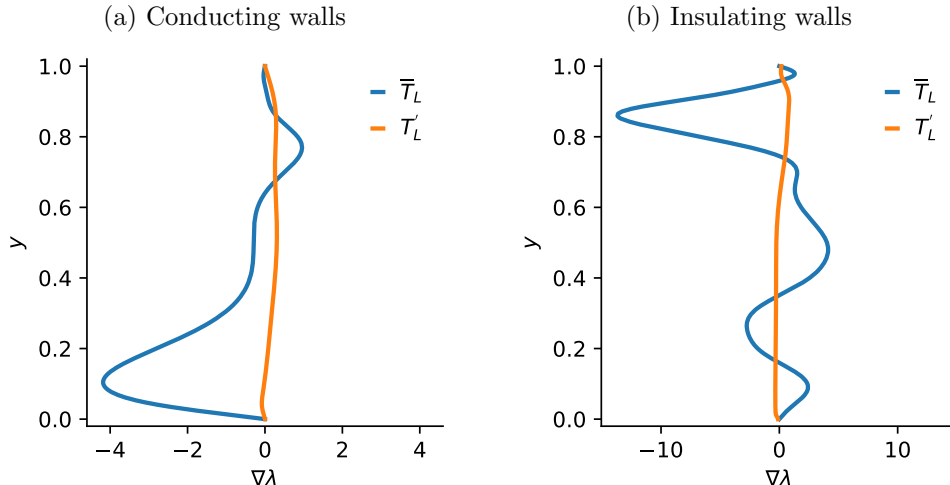
Figure 10: Sensitivity of eigenvalue with respect to steady and unsteady wall temperature forcing. Panels show (a) conducting horizontal walls ($Ra = 2.1 \times 10^6$) and (b) insulating horizontal walls ($Ra = 1.8 \times 10^8$).

The insulating horizontal wall configuration shows a peak sensitivity to steady forcing as the boundary layer departs towards the upper horizontal wall at $y \approx 0.85$ (Figure 10b). In high-aspect ratio cavities, Gadoin et al. [2001] proposed the flow is most sensitive to unsteady forcing at start of the boundary layer formation ($y/H \approx 1/3$), based on the adjoint global modes. In contrast, we find the flow is most receptive to being destabilized by unsteady forcing at $y \approx 0.9$ which corresponds to the peak value of $\nabla \hat{T}^+$, which is due to (7). The oscillating sensitivity of $\partial_{\overline{T}_L} \lambda$ between $0 < y < 0.7$ (Figure 10b) can be attributed to the internal waves that appear across the diagonal structure of the global modes (Figure 8). Compared to the conducting wall configuration (Figure 10a), the absolute value of peak sensitivity of the insulating walls to steady temperature forcing is three times larger (13.1 compared to 4.3). However, the integral of the sensitivity over the wall surface is slightly larger for the conducting wall configuration (-0.8) compared to the insulating wall configuration (-0.68). If practical limitations imposed that wall temperature forcing could only be applied to the entire boundary, it would therefore be more effective in the case of conducting boundary conditions.

4 Conclusions

We have studied the global stability of a differentially-heated square cavity under conducting and insulating horizontal boundary conditions, using the spectral element software Nektar++. To find the sensitivity of the eigenvalue with respect to wall temperature variations, we derived a continuous adjoint formulation. Wall temperature sensitivity profiles showed high sensitivity to steady forcing when in both flow configurations studied. The receptivity to unsteady wall temperature forcing was significantly lower than steady forcing, which agrees with the results of Qadri [2014] in low-density jets. In the insulating configuration, we observed a peak sensitivity to steady forcing on the upper region of the wall where the boundary layer detaches ($y \approx 0.9$), which acts to stabilize the flow. The peak sensitivity of the conducting configuration was at the onset of the boundary layer ($y \approx 0.1$), which also acted to stabilize the flow. The peak sensitivity value was higher for an insulating wall configuration, although the integral of sensitivity over the entire boundary was similar. As the adjoint global modes of the conducting wall problem were mainly focused along the horizontal boundaries, temperature or horizontal velocity forcing on the horizontal boundary may yield a stronger response in future research.

Appendix A   Continuous adjoint derivation

To find the sensitivity of the cost function, $\mathcal{J}$, to changes in the linear operator, we define a constrained optimisation problem where the adjoint variables are Lagrange multipliers constraining the solution to (4). The effect of changes in the wall temperature investigated in this study will act on the baseflow (considered in subsection A.1) and the linear perturbation (considered in this section). We write the

Lagrangian as

$$
\begin{aligned}
\mathcal{L} =& \mathcal{J} - \langle \boldsymbol{u}^+, \partial_t \boldsymbol{u}^{'} + \overline{\boldsymbol{u}} \cdot \nabla \boldsymbol{u}^{'} + \boldsymbol{u}^{'} \cdot \nabla \overline{\boldsymbol{u}} + \nabla p^{'} - Pr Ra^{-1/2} \nabla^2 \boldsymbol{u}^{'} + Pr T^{'} \boldsymbol{y} \rangle \\
& - \langle p^+, \nabla \cdot \boldsymbol{u}^{'} \rangle \\
& - \langle T^+, \partial_t T^{'} + \overline{\boldsymbol{u}} \cdot \nabla T^{'} + \boldsymbol{u}^{'} \cdot \nabla \overline{T} - Ra^{-1/2} \nabla^2 T^{'} \rangle \\
& - [T_L^+, T^{'}(\boldsymbol{x}_L, t) - T_L^{'}],
\end{aligned}
\tag{13}
$$

where we define the inner products as

$$
\langle a(x,t), b(x,t) \rangle = \int_\Omega a(x,t)^T b(x,t) d\Omega
\tag{14}
$$

$$
[a(x,t), b(x,t)] = \int_\Gamma a(x,t)^T b(x,t) d\Gamma.
\tag{15}
$$

Ω is the simulation domain (internal field) and Γ is a boundary.

To find the sensitivity of the cost function to changes in the linear operator, we must calculate partial derivatives of $\mathcal{L}$ with respect to $\boldsymbol{q}^+$ and $\boldsymbol{q}^{'}$. The sensitivity is

$$
\begin{aligned}
\delta \mathcal{L} =& \left\langle \frac{\delta \mathcal{L}}{\delta \boldsymbol{u}^{'}}, \delta \boldsymbol{u}^{'} \right\rangle + \left\langle \frac{\delta \mathcal{L}}{\delta p^{'}}, \delta p^{'} \right\rangle + \left\langle \frac{\delta \mathcal{L}}{\delta T^{'}}, \delta T^{'} \right\rangle + \left[\frac{\delta \mathcal{L}}{\delta T_L^{'}}, \delta T_L^{'} \right] \\
& + \left\langle \frac{\delta \mathcal{L}}{\delta \boldsymbol{u}^+}, \delta \boldsymbol{u}^+ \right\rangle + \left\langle \frac{\delta \mathcal{L}}{\delta p^+}, \delta p^+ \right\rangle + \left\langle \frac{\delta \mathcal{L}}{\delta T^+}, \delta T^+ \right\rangle + \left[\frac{\delta \mathcal{L}}{\delta T_L^+}, \delta T_L^+ \right].
\end{aligned}
\tag{16}
$$

Each term in (16) must then be expanded. The first term is therefore

$$
\begin{aligned}
\left\langle \frac{\delta \mathcal{L}}{\delta \boldsymbol{u}^{'}}, \delta \boldsymbol{u}^{'} \right\rangle =& \left\langle \frac{\delta \mathcal{J}}{\delta \boldsymbol{u}^{'}}, \delta \boldsymbol{u}^{'} \right\rangle \\
& - \left\langle \boldsymbol{u}^+, \partial_t \delta \boldsymbol{u}^{'} + \overline{\boldsymbol{u}} \cdot \nabla \delta \boldsymbol{u}^{'} + \delta \boldsymbol{u}^{'} \cdot \nabla \overline{\boldsymbol{u}} - Pr Ra^{-1/2} \nabla^2 \delta \boldsymbol{u}^{'} \right\rangle \\
& - \left\langle p^+, \nabla \delta \boldsymbol{u}^{'} \right\rangle \\
& - \left\langle T^+, \delta \boldsymbol{u}^{'} \cdot \nabla \overline{T} \right\rangle,
\end{aligned}
\tag{17}
$$

which can be written after integration by parts as

$$
\begin{aligned}
\left\langle \frac{\delta \mathcal{L}}{\delta \boldsymbol{u}^{'}}, \delta \boldsymbol{u}^{'} \right\rangle =& \left\langle \frac{\delta \mathcal{J}}{\delta \boldsymbol{u}^{'}}, \delta \boldsymbol{u}^{'} \right\rangle \\
& - \left\langle \partial_t \boldsymbol{u}^+ + \overline{\boldsymbol{u}} \cdot \nabla \boldsymbol{u}^+ + \boldsymbol{u}^+ \cdot \nabla \overline{\boldsymbol{u}} + \nabla p^+ + \frac{Pr}{\sqrt{Ra}} \nabla \boldsymbol{u}^+ + T^+ \nabla \overline{T}, \delta \boldsymbol{u}^{'} \right\rangle \\
& - \left[\frac{Pr}{\sqrt{Ra}} \nabla \boldsymbol{u}^+ \cdot \boldsymbol{n} + (\overline{\boldsymbol{u}} \boldsymbol{u}^+) \cdot \boldsymbol{n} + p^+ \boldsymbol{n} + T^+ T^{'} \boldsymbol{n}, \delta \boldsymbol{u}^{'} \right] + \left[\frac{Pr}{\sqrt{Ra}} \boldsymbol{u}^+, \nabla \delta \boldsymbol{u}^{'} \right].
\end{aligned}
\tag{18}
$$

The differentiation of the functional with respect to $\delta p^{'}$ is

$$
\left\langle \frac{\delta \mathcal{L}}{\delta p^{'}}, \delta p^{'} \right\rangle = \left\langle \frac{\delta \mathcal{J}}{\delta p^{'}}, \delta p^{'} \right\rangle - \left\langle \nabla \cdot \boldsymbol{u}^+, \delta p^{'} \right\rangle + \left[\boldsymbol{u}^+ \cdot \boldsymbol{n}, \delta p^{'} \right].
\tag{19}
$$

The differentiation of the functional with respect to $\delta T^{'}$ is

$$
\begin{aligned}
\left\langle \frac{\delta \mathcal{L}}{\delta T^{'}}, \delta T^{'} \right\rangle =& \left\langle \frac{\delta \mathcal{J}}{\delta T^{'}}, \delta T^{'} \right\rangle \\
& - \left\langle \boldsymbol{u}^+, Pr \boldsymbol{y} \delta T^{'} \right\rangle - \langle p^+, 0 \rangle \\
& - \left\langle T^+, \partial_t \delta T^{'} + \overline{\boldsymbol{u}} \cdot \nabla \delta T^{'} - \frac{1}{\sqrt{Ra}} \nabla^2 \delta T^{'} \right\rangle \\
& - \left[T_L^+, \delta T^{'} \right],
\end{aligned}
\tag{20}
$$

which after integration by parts gives us

$$\left\langle \frac{\delta \mathcal{L}}{\delta T'}, \delta T' \right\rangle = \left\langle \frac{\delta \mathcal{J}}{\delta T'}, \delta T' \right\rangle$$

$$- \left\langle \partial_t T^+ + \overline{\boldsymbol{u}} \cdot \nabla T^+ + \frac{1}{\sqrt{Ra}} \nabla^2 T^+ - Pr\left(\boldsymbol{y} \cdot \boldsymbol{u}^+\right), \delta T' \right\rangle$$

$$- \left[T^+ \overline{\boldsymbol{u}} \cdot \boldsymbol{n} + \frac{1}{\sqrt{Ra}} \nabla T^+ \cdot \boldsymbol{n} + T_L^+, \delta T' \right]$$

$$+ \left[\frac{1}{\sqrt{Ra}} T^+ \boldsymbol{n}, \nabla \delta T' \right]. \tag{21}$$

The differentiation of the functional with respect to $\delta T'_L$ is

$$\left[\frac{\delta \mathcal{L}}{\delta T'_L}, \delta T'_L \right] = \left[\frac{\delta \mathcal{J}}{\delta T'_L}, \delta T'_L \right] - \left[T_L^+, \delta T'_L \right]. \tag{22}$$

We aim to find the sensitivity of the eigenmode to changes in the wall temperature. We therefore set $\mathcal{J} = \lambda$, which substitute into (22) to give

$$\left[\frac{\delta \mathcal{L}}{\delta T'_L}, \delta T'_L \right] = \left[\partial_{T'_L} \lambda, \delta T'_L \right] - \left[T_L^+, \delta T'_L \right], \tag{23}$$

where at the boundary, we obtain

$$\left(\partial_{T'_L} \lambda \right)_\Gamma = T_L^+. \tag{24}$$

By setting $\overline{\boldsymbol{u}} = 0$ at the wall in (21) (terms in $[\cdot, \delta T']$) and combining with (24), we obtain the relationship below:

$$\partial_{T'_L} \lambda = T_L^+ = \frac{1}{\sqrt{Ra}} \nabla T^+ \cdot \boldsymbol{n}, \tag{25}$$

which can be obtained from the adjoint global mode [Qadri, 2014]. This is in line with Meliga et al. [2010], who studied sensitivity to wall temperature (T_w) perturbations in compressible flow. They derived the following relationship:

$$\partial_{T_w} \lambda = T_w^+ = \frac{\gamma}{PrRe} \nabla T^+ \cdot \boldsymbol{n}, \tag{26}$$

where $\gamma/(PrRe)$ is the diffusion coefficient in the temperature transport equation.

A.1 Base flow sensitivity

Steady variations in the wall temperature implies the Lagrangian must be extended to include so called "adjoint baseflow" fields, $\overline{\boldsymbol{q}}^+$. The functional is therefore

$$\mathcal{L} = \lambda - \langle \boldsymbol{u}^+, \lambda \hat{\boldsymbol{u}} + \overline{\boldsymbol{u}} \cdot \nabla \hat{\boldsymbol{u}} + \hat{\boldsymbol{u}} \cdot \nabla \overline{\boldsymbol{u}} + \nabla \hat{p} - PrRa^{-1/2} \nabla^2 \hat{\boldsymbol{u}} + Pr\hat{T}\boldsymbol{y} \rangle$$

$$- \langle p^+, \nabla \cdot \hat{\boldsymbol{u}} \rangle$$

$$- \langle T^+, \lambda \hat{T} + \overline{\boldsymbol{u}} \cdot \nabla \hat{T} + \hat{\boldsymbol{u}} \cdot \nabla \overline{T} - Ra^{-1/2} \nabla^2 \hat{T} \rangle$$

$$- \langle \overline{\boldsymbol{u}}^+, \overline{\boldsymbol{u}} \cdot \nabla \overline{\boldsymbol{u}} + \nabla \overline{p} - PrRa^{-1/2} \nabla^2 \overline{\boldsymbol{u}} + Pr\overline{T}\boldsymbol{y} \rangle \tag{27}$$

$$- \langle \overline{p}^+, \nabla \cdot \overline{\boldsymbol{u}} \rangle$$

$$- \langle \overline{T}^+, \overline{\boldsymbol{u}} \cdot \nabla \overline{T} - Ra^{-1/2} \nabla^2 \overline{T} \rangle$$

$$- [\overline{T}_L^+, \overline{T}(\boldsymbol{x}_L, t) - \overline{T}_L].$$

To find the sensitivity of the cost function to changes in the linear operator, we must calculate partial derivatives of $\mathcal{L}$ with respect to $\boldsymbol{q}^+$ and $\boldsymbol{q}'$. The sensitivity is

$$\delta\mathcal{L} = \left\langle \frac{\delta\mathcal{L}}{\delta\boldsymbol{u}'}, \delta\boldsymbol{u}' \right\rangle + \left\langle \frac{\delta\mathcal{L}}{\delta p'}, \delta p' \right\rangle + \left\langle \frac{\delta\mathcal{L}}{\delta T'}, \delta T' \right\rangle + \left\langle \frac{\delta\mathcal{L}}{\delta\overline{\boldsymbol{u}}}, \delta\overline{\boldsymbol{u}} \right\rangle + \left\langle \frac{\delta\mathcal{L}}{\delta\overline{T}}, \delta\overline{T} \right\rangle$$

$$+ \left[\frac{\delta\mathcal{L}}{\delta T'_L}, \delta T'_L \right] + \left[\frac{\delta\mathcal{L}}{\delta\overline{T}_L}, \delta\overline{T}_L \right]$$

$$+ \left\langle \frac{\delta\mathcal{L}}{\delta\boldsymbol{u}^+}, \delta\boldsymbol{u}^+ \right\rangle + \left\langle \frac{\delta\mathcal{L}}{\delta p^+}, \delta p^+ \right\rangle + \left\langle \frac{\delta\mathcal{L}}{\delta T^+}, \delta T^+ \right\rangle + \left\langle \frac{\delta\mathcal{L}^+}{\delta\overline{\boldsymbol{u}}}, \delta\overline{\boldsymbol{u}}^+ \right\rangle + \left\langle \frac{\delta\mathcal{L}^+}{\delta\overline{T}}, \delta\overline{T}^+ \right\rangle \quad (28)$$

$$+ \left[\frac{\delta\mathcal{L}}{\delta T_L^+}, \delta T_L^+ \right] + \left[\frac{\delta\mathcal{L}}{\delta\overline{T}_L^+}, \delta\overline{T}_L^+ \right]$$

Each term in (28) must then be expanded. The first base flow term is therefore

$$\left\langle \frac{\delta\mathcal{L}}{\delta\overline{\boldsymbol{u}}}, \delta\overline{\boldsymbol{u}} \right\rangle = \partial_{\delta\overline{\boldsymbol{u}}}\lambda - \langle \boldsymbol{u}^+, \delta\overline{\boldsymbol{u}} \cdot \nabla\hat{\boldsymbol{u}} + \hat{\boldsymbol{u}} \cdot \nabla\delta\overline{\boldsymbol{u}} \rangle$$

$$- \langle T^+, \delta\overline{\boldsymbol{u}} \cdot \nabla\hat{T} \rangle$$

$$- \langle \overline{\boldsymbol{u}}^+, \overline{\boldsymbol{u}} \cdot \nabla\delta\overline{\boldsymbol{u}} + \delta\overline{\boldsymbol{u}} \cdot \nabla\overline{\boldsymbol{u}} - PrRa^{-1/2}\nabla^2\delta\overline{\boldsymbol{u}} \rangle \quad (29)$$

$$- \langle \overline{p}^+, \nabla \cdot \delta\overline{\boldsymbol{u}} \rangle$$

$$- \langle \overline{T}^+, \delta\overline{\boldsymbol{u}} \cdot \nabla\overline{T} \rangle,$$

which, after integration by parts gives

$$\left\langle \frac{\delta\mathcal{L}}{\delta\overline{\boldsymbol{u}}}, \delta\overline{\boldsymbol{u}} \right\rangle = \partial_{\delta\overline{\boldsymbol{u}}}\lambda$$

$$- \left\langle \boldsymbol{u}^+ \cdot \nabla\hat{\boldsymbol{u}} + \hat{\boldsymbol{u}} \cdot \nabla\boldsymbol{u}^+ + T^+\nabla\hat{T} + \overline{T}^+\nabla\overline{T} + \overline{\boldsymbol{u}}^+ \cdot \nabla\overline{\boldsymbol{u}} + \overline{\boldsymbol{u}} \cdot \nabla\overline{\boldsymbol{u}}^+ - \frac{Pr}{\sqrt{Ra}}\nabla^2\overline{\boldsymbol{u}}^+ + \nabla\overline{p}^+, \delta\overline{\boldsymbol{u}} \right\rangle. \quad (30)$$

The variations with respect to baseflow temperature can be expanded as

$$\left\langle \frac{\delta\mathcal{L}}{\delta\overline{T}}, \delta\overline{T} \right\rangle = \partial_{\delta\overline{T}}\lambda - \langle T^+, \hat{\boldsymbol{u}} \cdot \nabla\delta\overline{T} \rangle$$

$$- \langle \overline{\boldsymbol{u}}^+, Pr\boldsymbol{y}\delta\overline{T} \rangle$$

$$- \langle \overline{T}^+, \overline{\boldsymbol{u}} \cdot \nabla\delta\overline{T} - Ra^{-1/2}\nabla^2\delta\overline{T} \rangle \quad (31)$$

$$- \left[\overline{T}_L^+, \delta\overline{T} \right],$$

which after integration by parts gives

$$\left\langle \frac{\delta\mathcal{L}}{\delta\overline{T}}, \delta\overline{T} \right\rangle = \partial_{\delta\overline{T}}\lambda - \langle T^+, \hat{\boldsymbol{u}} \cdot \nabla\delta\overline{T} \rangle$$

$$- \left\langle \hat{\boldsymbol{u}} \cdot \nabla T^+ + \overline{\boldsymbol{u}} \cdot \nabla\overline{T}^+ + Pr(\boldsymbol{y} \cdot \overline{\boldsymbol{u}}^+) - Ra^{-1/2}\nabla^2\overline{T}^+, \delta\hat{T} \right\rangle \quad (32)$$

$$- \left[Ra^{-1/2}\nabla\overline{T}^+ + \overline{T}_L^+, \delta\overline{T} \right].$$

This gives the following equations for the adjoint base flow:

$$\nabla \cdot \overline{\boldsymbol{u}}^+ = 0, \quad (33a)$$

$$\overline{\boldsymbol{u}}^+ \cdot \nabla\overline{\boldsymbol{u}} + \overline{\boldsymbol{u}} \cdot \nabla\overline{\boldsymbol{u}}^+ = -\hat{\boldsymbol{u}} \cdot \nabla\hat{\boldsymbol{u}}^+ - \hat{\boldsymbol{u}}^+ \cdot \nabla\hat{\boldsymbol{u}} - \hat{T}^+\nabla\hat{T} - \overline{T}^+\nabla\overline{T} + \frac{Pr}{\sqrt{Ra}}\nabla^2\overline{\boldsymbol{u}}^+ - \nabla\overline{p}^+, \quad (33b)$$

$$\overline{\boldsymbol{u}} \cdot \nabla\overline{T}^+ = -\hat{\boldsymbol{u}} \cdot \nabla T^+ + \frac{1}{\sqrt{Ra}}\nabla^2\overline{T}^+ + Pr(\boldsymbol{y} \cdot \overline{\boldsymbol{u}}^+), \quad (33c)$$

where the sensitivity gradient can be computed from the temperature gradient at the boundary as

$$\overline{T}_L^+ = \frac{1}{\sqrt{Ra}}\nabla\overline{T}^+ = \partial_{\delta\overline{T}_L}\lambda. \quad (34)$$

12

Appendix B   Proxy-app usage details

The global mode forcing in (8) has been implemented in our proxy-app, and can be called in the Nektar++ xml file as:

```xml
<FUNCTION NAME="AdjointGlobalMode">
    <F VAR="u,v,T" FILE="domain_mesh_adjoint_globalmode_eig_1.bse" />
</FUNCTION>
<FUNCTION NAME="DirectGlobalMode">
    <F VAR="u,v,T" FILE="domain_mesh_direct_globalmode_eig_0.bse" />
</FUNCTION>


<FORCING>
    ...
    <FORCE TYPE="GlobalModeForcing">
        <BODYFORCE> GlobalModeForcing </BODYFORCE>
    </FORCE>
    ...
</FORCING>
```

This required the addition of a new forcing term in the modified Navier-Stokes solver (`ForcingGlobalMode.cpp`, alongside the necessary file). This consists of two steps at initialisation: (i) read adjoint and direct global modes; (ii) apply normalisations in (9) and (10). Then, at each step the forcing terms are computed and applied. For simplicity, this is done at each step as this was closer to the existing adjoint-related code such as `AdjointAdvection.cpp` and other forcing terms. However, since the fields are stationary (they are obtained from previously computed flows), the calculation of derivatives and summation of each term could be done at the beginning (unless a time-varying global mode was used).

References

E. Åkervik, L. Brandt, D. S. Henningson, J. Hœpffner, O. Marxen, and P. Schlatter. Steady solutions of the navier-stokes equations by selective frequency damping. *Physics of fluids*, 18(6), 2006.

D. Barkley, H. M. Blackburn, and S. J. Sherwin. Direct optimal growth analysis for timesteppers. *International journal for numerical methods in fluids*, 57(9):1435–1458, 2008.

C. D. Cantwell, D. Moxey, A. Comerford, A. Bolis, G. Rocco, G. Mengaldo, D. De Grazia, S. Yakovlev, J.-E. Lombard, D. Ekelschot, et al. Nektar++: An open-source spectral/hp element framework. *Computer physics communications*, 192:205–219, 2015.

E. Gadoin, P. Le Quéré, and O. Daube. A general methodology for investigating flow instabilities in complex geometries: application to natural convection in enclosures. *International Journal for Numerical methods in fluids*, 37(2):175–208, 2001.

F. Giannetti and P. Luchini. Structural sensitivity of the first instability of the cylinder wake. *Journal of Fluid Mechanics*, 581:167–197, 2007.

B. E. Jordi, C. J. Cotter, and S. J. Sherwin. An adaptive selective frequency damping method. *Physics of Fluids*, 27(9), 2015.

A. Kord and J. Capecelatro. Optimal perturbations for controlling the growth of a Rayleigh–Taylor instability. *Journal of Fluid Mechanics*, 876:150–185, 2019.

P. Le Quéré and M. Behnia. From onset of unsteadiness to chaos in a differentially heated square cavity. *Journal of fluid mechanics*, 359:81–107, 1998.

R. B. Lehoucq, D. C. Sorensen, and C. Yang. *ARPACK users' guide: solution of large-scale eigenvalue problems with implicitly restarted Arnoldi methods*. SIAM, 1998.

T. Luce. Realizing steady-state tokamak operation for fusion energy. *Physics of Plasmas*, 18(3):030501, 2011.

P. Luchini and A. Bottaro. Adjoint equations in stability analysis. *Annual Review of fluid mechanics*, 46:493–517, 2014.

L. Magri. Adjoint methods as design tools in thermoacoustics. *Applied mechanics reviews*, 71(2), 2019.

P. Meliga, D. Sipp, and J.-M. Chomaz. Open-loop control of compressible afterbody flows using adjoint methods. *Physics of Fluids*, 22(5), 2010.

S. Mordijck. Taking control of fusion reactor instabilities. *Physics*, 15:154, 2022.

D. Moxey, C. D. Cantwell, Y. Bao, A. Cassinelli, G. Castiglioni, S. Chun, E. Juda, E. Kazemi, K. Lackhove, J. Marcon, et al. Nektar++: Enhancing the capability and application of high-fidelity spectral/hp element methods. *Computer Physics Communications*, 249:107110, 2020.

K. H. Nordlund et al. European research roadmap to the realisation of fusion energy. 2018. URL `https://euro-fusion.org/wp-content/uploads/2022/10/2018_Research_roadmap_long_version_01.pdf`.

U. A. Qadri. *Global stability and control of swirling jets and flames.* PhD thesis, University of Cambridge, 2014. URL `https://www.repository.cam.ac.uk/handle/1810/245143`.

U. A. Qadri, L. Magri, M. Ihme, and P. J. Schmid. Using adjoint-based optimization to enhance ignition in non-premixed jets. *Proceedings of the Royal Society A*, 477(2245):20200472, 2021.

C. Saglietti, P. Schlatter, A. Monokrousos, and D. S. Henningson. Adjoint optimization of natural convection problems: differentially heated cavity. *Theoretical and Computational Fluid Dynamics*, 31: 537–553, 2017.

P. J. Schmid and L. Brandt. Analysis of fluid systems: Stability, receptivity, sensitivity. *Applied Mechanics Review*, 66(2):024803, 2014.

E. Threlfall, S. Powell, and W. Arter. Uncertainty quantification code integration, acceptance and operation 1. techreport CD/EXCALIBUR-FMS/0073-M5c1, UK Atomic Energy Authority, 2023.

R. Vishnampet, D. J. Bodony, and J. B. Freund. A practical discrete-adjoint method for high-fidelity compressible turbulence simulations. *Journal of Computational Physics*, 285:173–192, 2015.

J. Williams, U. A. Qadri, and S. Thorne. Review of adjoint method in plasma physics for NEPTUNE. Technical Report 2068625-TN-08, UKAEA, 2023.